THE JOURNAL OF PHYSICAL CHEMISTRY C

Article

Cite This: J. Phys. Chem. C 2018, 122, 5759−5766

pubs.acs.org/JPCC

Temperature- and Size-Dependent Exciton Dynamics in PbS Colloidal Quantum Dot Thin Films Using Combined Photoluminescence Spectroscopy and Photocarrier Radiometry

Jing Wang,[†,*] Andreas Mandelis,[†,‡] Qiming Sun,[†] Bincheng Li,[†] and Chunming Gao[†]

[†]School of Optoelectronic Information, University of Electronic Science and Technology of China, Chengdu, Sichuan 610054, China

[‡]Center for Advanced Diffusion-Wave and Photoacoustic Technologies (CADIPT), Department of Mechanical and Industrial Engineering, University of Toronto, Toronto M5S 3G8, Canada

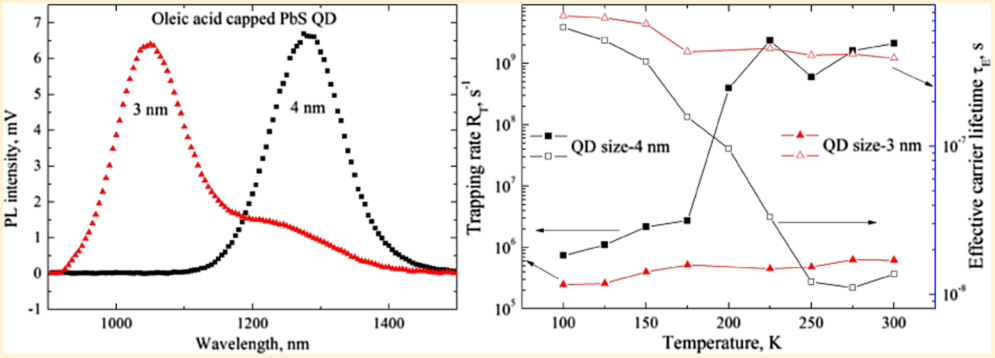

ABSTRACT: Lead salt colloidal quantum dots (CQDs) are promising active components for applications in electronic and optoelectronic devices such as photodetectors, light-emitting diodes, and solar cells. Detailed understanding of exciton dynamics in these nanocrystalline films is crucial for their practical applications. Photocarrier radiometry (PCR) is a dynamic spectrally integrated frequency-domain photoluminescence (PL) method, the spectral bandwidth of which is gated to eliminate thermal infrared photons due to nonradiative recombination. On the other hand, PL spectroscopy is a steady-state method that offers complementary spectrally resolved information. Combined PL temperature spectra and PCR temperature and frequency measurements were applied to PbS CQD thin films capped with oleic acid. Enhanced PL intensities at high temperatures originating in thermally activated exciton transfer from trap to exciton states were found in two samples consisting of two different sizes of quantum dots. A theoretical excitonic diffusion-wave PCR model was developed to extract exciton recombination lifetimes, hopping diffusivity, and trapping rates. It was found that the smaller size (3 nm) quantum dots exhibit considerably improved excitonic transport properties compared to the larger quantum dots (4 nm), including longer effective lifetime, higher degree of localization (diffusion length), and smaller trapping and thermal emission rates. Therefore, small-size quantum dots are more suitable for optoelectronic device applications.

1. INTRODUCTION

Colloidal quantum dots (CQDs) made of narrow-band gap IV−VI semiconductors, such as PbS and PbSe, have been excellent candidates for electronic and optoelectronic devices such as photodetectors,[1,2] light-emitting diodes,[3,4] and solar cells[5,6] because of their ability to effectively absorb and emit light in the near-infrared region. Clear and detailed understanding of the energy diffusion and energy-transfer processes is crucial for improving material properties and the associated device performance. Although intense efforts have been made on probing carrier dynamics in lead salt CQDs by several research groups around the world, differences among samples and complex surface passivation conditions make it difficult to achieve a clear and consistent physical picture of the optoelectronic properties in QDs.

The large surface-to-volume ratio, an inherent feature of QDs, introduces large densities of surface defects, which trap charge carriers.[7] Photoluminescence (PL) spectra and temperature-dependent PL have been applied to study the carrier dynamics involving trap states.[8−17] Charge-transfer mechanisms based on switching from Efros−Shklovskii variable-range hopping to nearest neighbor hopping with increased temperatures have been studied with thermal PL measurements.[8,9] Organic and inorganic surface passivation methods that greatly improve the optoelectronic properties of QDs were tested with the help of PL spectra.[10−12] The fact that charge carrier transport occurring in QD ensembles is governed by diffusion-controlled trap-assisted recombination has been supported by size- and/or temperature-dependent PL results.[13−15] Litvin et al. found that QDs of different sizes exhibit entirely different temperature depend-

Received: December 4, 2017
Revised: February 16, 2018
Published: February 20, 2018

DOI: 10.1021/acs.jpcc.7b11933
J. Phys. Chem. C 2018, 122, 5759−5766

encies of their PL properties because of an in-gap state of size-dependent energy, which is associated with surface defect states.[15]

Anomalous temperature-dependent PL properties have been assigned to trap state effects.[18−20] Rinnerbauer et al. found that increased PL intensity in closed-packed PbS nanocrystals at high temperatures is caused by thermal activation and energy transfer from surface to exciton states.[18] Andreakou et al. observed an anomalously enhanced PL intensity in PbS CQDs in the temperature range from 180 to 250 K, which was due to thermally activated trapped carriers populating dark and bright states.[19] Ma et al. observed an anomalous PL temperature dependence in self-assembled InGaN QDs and found that the integrated PL intensity shows a dramatic increase in the temperature range from 160 to 215 K. A theoretical model of temperature-induced carrier redistribution from shallow and deep localized states was used to interpret this phenomenon.[20]

Photocarrier radiometry (PCR), as a dynamic spectrally integrated frequency-domain PL modality,[21] has been applied to analyze radiative and nonradiative relaxation processes as well as exciton transport hopping properties in PbS CQDs.[22,23] In this work, combined temperature-dependent PL spectra and PCR temperature and frequency scans were performed to elucidate the exciton dynamics in oleic acid-capped PbS QDs.

2. MATERIALS AND EXPERIMENTAL SETUP

Two thin-film PbS CQD samples with mean diameters of 3 nm (sample A) and 4 nm (sample B) were studied for the purpose of probing temperature-dependent exciton dynamics in QDs. Both samples were capped with oleic acid, and the film thickness was approximately 300 nm. Each tested sample was placed on a Linkam LTS420 cryogenic stage, which allows maintaining a constant temperature in the 77−300 K range. The schematic diagram of the PCR experimental setup was similar to those in our previous publications[22,23] and is shown in Figure 1. An 808

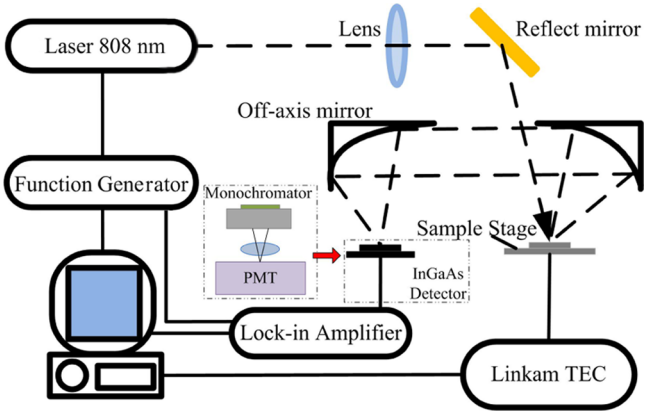

Figure 1. Schematic diagram of the experimental setup.

nm, 100 mW diode laser with a beam diameter of ca. 0.1 mm was square-wave-modulated using a function generator. A 1 μm long-pass filter was placed in front of the InGaAs photodetector to block the excitation beam. PCR temperature scans and laser modulation frequency scans were performed to characterize charge carrier kinetic processes in PbS CQD thin films. The temperature scan range was from 100 to 300 K, whereas the frequency scan range was from 10 Hz to 500 kHz. By substituting a monochromator and a photomultiplier tube for the InGaAs photodetector, the PCR system was converted into a typical steady-state PL spectroscopy system, as shown within the dashed box in Figure 1. The range of the PL spectra was from 900 to 1500 nm.

3. RESULTS AND DISCUSSION

3.1. Temperature-Dependent PL Spectra. The PL spectra at five temperatures 300, 250, 200, 150, and 100 K for both samples A and B are shown in Figures 2 and 3, respectively.

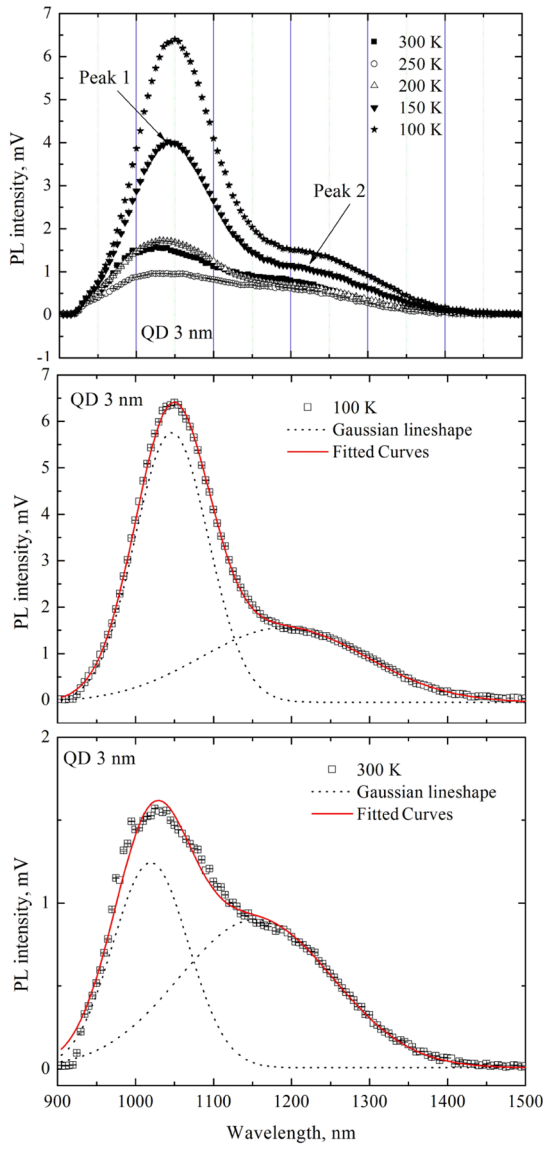

Figure 2. PL spectra of sample A at various temperatures and line shape best-fit curves.

Two emission bands are evident in sample A (Figure 2). According to the reported values of PbS QD band edge,[24] the shorter wavelength peak is emitted from the band edge, whereas the lower-energy secondary peak is emitted from defect states.[23,25] A line shape analysis of the steady-state PL spectra was performed with a superposition of two PL bands. The line shape of each PL band was assumed to be Gaussian. Solid lines in Figure 2 denote the results of the line shape analysis, and dashed lines indicate each Gaussian line shape of the two PL bands. It is noted that the results of the line shape analysis yield excellent fits

DOI: 10.1021/acs.jpcc.7b11933
J. Phys. Chem. C 2018, 122, 5759−5766

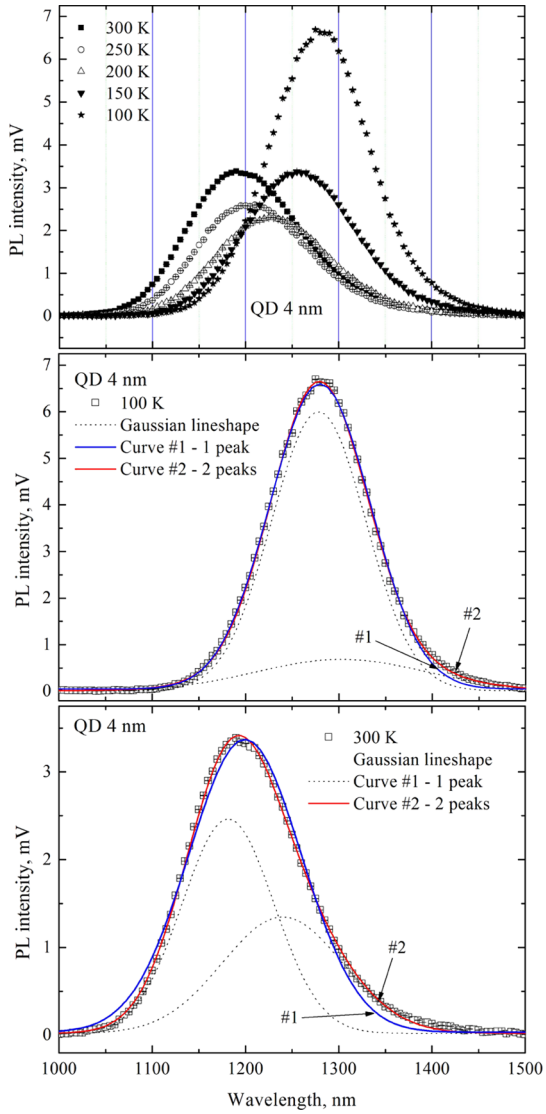

Figure 3. PL spectra of sample B at various temperatures and line shape best-fit curves.

to the experimental PL spectra. The extracted spectral peak positions and peak intensities for sample A are listed in Table 1.

As it was hard to identify whether the line shapes of the PL spectra for sample B could be described by one or two superposed Gaussians, both line shapes were used to fit the spectra at various temperatures. Solid lines #1 in Figure 3 denote one-Gaussian line shape, and solid lines #2 represent the results of line shape fits with two Gaussians. The best-fit variances for one Gaussian are listed in Table 2, which also includes the fitted peak positions and peak intensities. In the case of fitting the data with two Gaussians, the extracted spectral positions of the longer wavelength peak 2 were found to change nonmonotonically with temperature, whereas the goodness of the line shape fitting did not show any distinct advantage compared with the one-Gaussian fitting. Therefore, henceforth only one PL band was considered for this PbS CQD thin film.

Table 2. Summary of Measurements of the PL Peak Positions and Intensities of Sample B Fitted with One-Gaussian Line Shape

temperature, K	position, nm	intensity, mV	variance
100	1279.8 ± 0.17	$6.55 \pm 1.2 \times 10^{-4}$	1.1×10^{-3}
150	1258.9 ± 0.22	$3.32 \pm 1.2 \times 10^{-4}$	1.4×10^{-3}
200	1230.0 ± 0.32	$2.27 \pm 1.1 \times 10^{-4}$	2.9×10^{-3}
250	1209.2 ± 0.41	$2.58 \pm 1.8 \times 10^{-4}$	4.1×10^{-3}
300	1199.5 ± 0.46	$3.34 \pm 3.8 \times 10^{-4}$	4.8×10^{-3}

Plots of the PL peak energy positions versus temperatures for the two samples are shown in Figure 4. The temperature dependence of the PL peak positions can be well-described by the Varshni equation.[26,27]

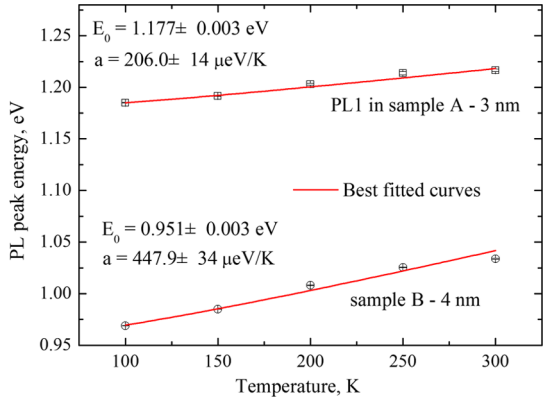

Figure 4. PL peak energy vs temperature of band gap emission of PbS CQD thin films. The solid lines represent a fit to the Varshni eq 1.

$$E(T) = E_0 + \alpha \frac{T^2}{T + \theta_D} \quad (1)$$

where E_0 represents the band gap at $T = 0$ K (in the case of QDs, E_0 should be the energy of the lowest 1S−1S exciton state); θ_D is a constant of the order magnitude of the semiconductor material Debye temperature, which is 145 K for bulk PbS;[28] and α is the band gap energy temperature coefficient. The obtained value of α for the 3 nm CQDs shown in Figure 4 is smaller than that for the 4 nm CQDs, and they are both smaller than the value in bulk PbS, which is 520 μeV/K. These results are consistent with the reports by Olkhovets et al.[29] and Kigel et al.,[26] in which α increases monotonically with QD size. Furthermore, Kigel et al. reported values similar to those we found here for similar QD sizes.[26]

Table 1. Summary of Measurements of the PL Peak Positions and Intensities of Sample A

temperature, K	peak 1		peak 2	
	position, nm	intensity, mV	position, nm	intensity, mV
100	1046.4 ± 0.19	$5.81 \pm 3.5 \times 10^{-3}$	1190.2 ± 3.40	$1.61 \pm 5.6 \times 10^{-4}$
150	1040.7 ± 0.35	$3.61 \pm 3.8 \times 10^{-4}$	1184.6 ± 4.79	$1.19 \pm 2.0 \times 10^{-4}$
200	1030.9 ± 0.86	$1.51 \pm 6.5 \times 10^{-4}$	1177.6 ± 5.94	$0.72 \pm 4.7 \times 10^{-4}$
250	1021.8 ± 1.39	$0.75 \pm 6.9 \times 10^{-4}$	1167.7 ± 5.23	$0.65 \pm 1.6 \times 10^{-4}$
300	1019.4 ± 0.98	$1.24 \pm 5.3 \times 10^{-4}$	1154.2 ± 6.30	$0.89 \pm 4.4 \times 10^{-4}$

DOI: 10.1021/acs.jpcc.7b11933
J. Phys. Chem. C 2018, 122, 5759−5766

Figure 5 shows the temperature-dependent PL peak intensities extracted from Figures 2 and 3. It is observed that with increased

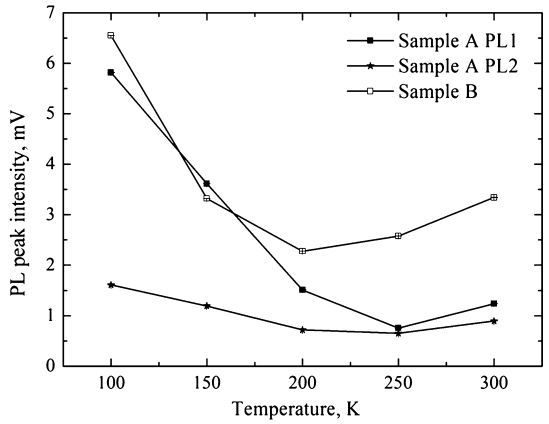

Figure 5. PL peak intensities vs temperature of PbS CQD thin films.

temperature, the peak intensities first decrease and then increase for both samples. According to similar phenomena reported for PbS CQDs[18,19] and InGaN QDs,[20] the high-temperature peak enhancement can be caused by thermally activated exciton redistribution from trap states to ground exciton states. Specifically for sample A, both PL peak 1 and peak 2 are enhanced at high temperatures, which are indicative that there are thermally activated exciton redistributions from "dark" trap states to "emission" states.

The excited-state energetic manifold for PbS CQDs is shown in Figure 6[22] where the lowest 1S−1S exciton states split into a

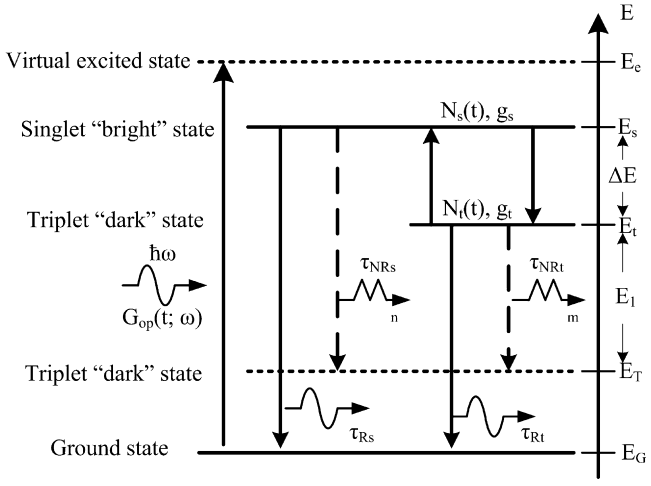

Figure 6. Excited-state manifold of PbS exciton in the singlet−triplet energy range. Photon emission: sine wave arrows indicate radiative emission processes. Phonon emission: sawtooth arrows indicate nonradiative decay processes in the presence of photocarrier exciton traps (from ref 22).

triplet dark and a higher energy singlet "bright" state. Here, radiative and nonradiative pathways are marked with corresponding singlet and triplet lifetimes τ_{Rs} and τ_{Rt} (radiative) and τ_{NRs} and τ_{NRt} (nonradiative), respectively. Also, shown are m and n phonons emitted by the nonradiative transitions from the singlet and triplet states, respectively, to trap states.

3.2. Temperature-Dependent PCR Signals. While Figure 5 shows the steady thermophotonic properties of the spectrally resolved PL emission peak intensities in the two samples, the temperature-dependent PCR amplitude represents the dynamic temperature response of the integrated PL intensities in QDs. Figure 7 shows the Arrhenius plots of the PCR amplitude across temperatures ranging from 100 to 300 K for both samples. Dynamic radiative (PL) emission enhancements at high temperatures were found at all laser modulation frequencies, only two of which are shown here. In general, eq 2 is used to describe the temperature-dependent PCR amplitude/intensity of CQDs:[30]

$$I(T) = \frac{I_0}{1 + A_1\, e^{-E_1/k_B T}} \tag{2}$$

where I_0 is a normalizing factor, $E_1 = E_t - E_T$ is the activation energy of the process that transfers excitons from the (assumed single-level) trap state E_T to the lowest exciton state E_t, and A_1 is the carrier transition probability for this process. The activation energy is the energy difference between the original and the final energy states within a carrier transition process.

In the present case, however, the exciton transfer processes are more complicated than the simple physical process described by eq 2. Thermally activated exciton redistributions from trap states to emission states exist in our samples in addition to the optically excited photocarriers either in the form of excitons or their dissociated free-carrier products, as per the PL spectra. As shown in the excited-state manifold in Figure 6, the radiative emission rate from the lowest excited bright state can be written as

$$I(t) = \frac{N_R(T)}{\tau_R} = \frac{N_t(T) + N_s(T)}{\tau_R} = \frac{N_t(T)}{\tau_R} (1 + A_2\, e^{-\Delta E/k_B T}) \tag{3}$$

where $A_2 = g_s = g_t = 1/3$ is the degeneracy ratio between singlet and triplet states. The component $\Delta N_T(T) = N_T \exp[-(E_t - E_T)/k_B T]$ of the population $N_t = N_{t0} + \Delta N_T$ of the triplet state thermally supplied by the trapping state(s)[31] further decreases as a result of nonradiative de-excitation of the thermal carriers into the same and other trap states, rather than statistically becoming redistributed into the radiative active singlet (bright) state E_s and the triplet state E_t. Therefore, the population of the triplet state in the presence of "leakage" into nonradiative states can be expressed as

$$N_t(T) = \frac{N_{t0}}{1 + \left(\frac{N_T}{N_{t0}}\right) \exp[-(E_t - E_T)/k_B T]} \tag{4}$$

Combining eqs 3 and 4 and simplifying the notation yield modified eq 2

$$I(T) = I_0 \left(\frac{1 + A_2\, e^{-E_2/k_B T}}{1 + A_1\, e^{-E_1/k_B T}} \right) \tag{5}$$

Here, $E_2 \equiv \Delta E$ is the energy gap between the dark states and the lowest exciton states and $I_0 = N_{t0}/\tau_R$. Fitting the temperature-dependent PCR amplitude results with eq 5, the activation energies of those two kinds of transitions which have different transition directions were calculated. The solid lines in Figure 7 are the best-fitted curves. It was found that the activation energy E_2 of the process that transfers excitons from the triplet state to the singlet state is about 30 meV in sample B, which is only half of that in sample A. Furthermore, the higher trap-to-triplet (dark) state activation energy E_1 for sample B than that for sample A at a

DOI: 10.1021/acs.jpcc.7b11933
J. Phys. Chem. C 2018, 122, 5759−5766

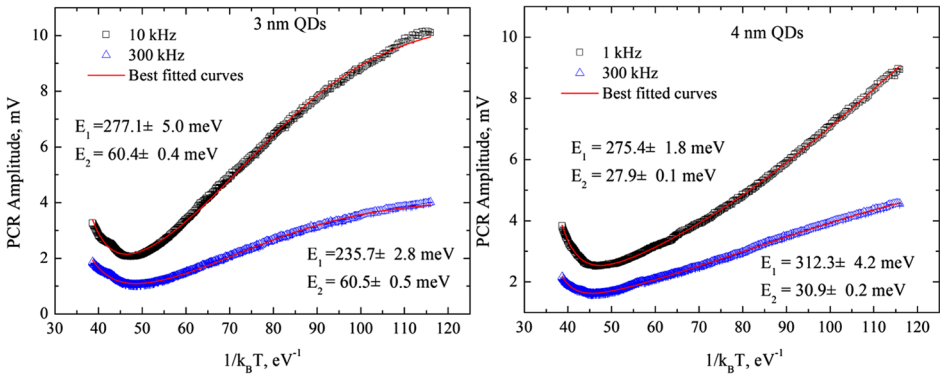

Figure 7. PCR photothermal amplitude spectra (temperature scan curves) for both PbS CQD samples at various frequencies. Best-fitted curves were calculated from eq 3. Left: sample A and right: sample B.

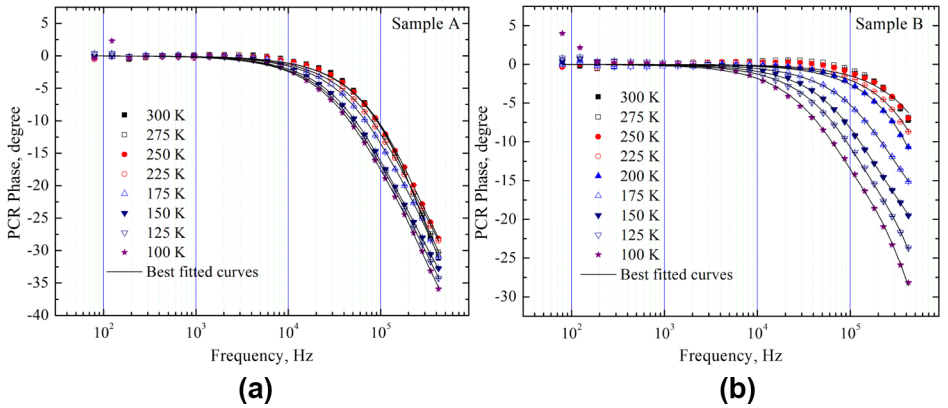

Figure 8. Phase diagrams of PCR frequency scans at various temperatures. Best-fitted curves were calculated from eq 9. (a) sample A and (b) sample B.

300 kHz modulation frequency (commensurate with the inverse of the effective carrier lifetimes; Figure 9a) is indicative that excitons in sample B have a larger barrier to radiative emission through redistribution into the bright singlet state and thus higher nonradiative decay probability from the original trap states than excitons in sample A. The redistribution causing enhanced PL intensities at high temperatures originates from trap states with large energy gap(s) > 200 meV from the lowest radiative emission states. Lagoudakis et al.[19] have reported exciton redistribution with an activation energy of ca. 100 meV for PbS CQDs with a 3.2 nm size. Ma et al.[20] also reported localized excitons with energies of 185 and 100 meV, which can be thermally activated.

3.3. PCR Frequency Response Analysis. Recently, a trap-state-mediated carrier hopping transport rate model was developed by Hu et al.[23] based on the excited-state manifold in Figure 6, from which multiple exciton (or dissociated carrier) transport parameters can be extracted. For the harmonic laser excitation at frequency $f = \omega/2\pi$, the frequency-domain carrier rate equation is reproduced here.

$$\frac{d^2N_t(x,\omega)}{dx^2} - \frac{1}{D_h(T)}\left[i\omega + \frac{1}{\tau_E(T)} - \frac{R_T}{[1+A(T)][1+i\omega\tau_i(T;x,\omega)]}\right]N_t(x,\omega) = -\frac{G_0\beta\, e^{-\beta x}}{D_h(T)[1+A(T)]} \quad (6)$$

where N_t is the photocarrier population in the triplet dark state, D_h is the exciton or dissociated carrier hopping diffusivity, τ_i is defined as $1/\tau_i(T) = e_i(T)$, where e_i is the thermal emission rate of carriers from a single trap level, R_T is defined as the carrier trapping rate, and G_0 is the photocarrier generation rate. $A(T) = A_2\, e^{-E_2/k_BT}$; ω is the modulation angular frequency and β is the optical absorption coefficient of the CQDs at the laser excitation wavelength, $\tau_E(T)$ is the effective carrier lifetime, which is defined as extremely

$$\frac{1}{\tau_E(T)} \equiv \frac{1}{1+A(T)}\left[\frac{1}{\tau_t(T)} + \frac{A(T)}{\tau_s(T)}\right]$$

and τ_t and τ_s are the triplet and singlet lifetimes, respectively.

For CQD thin films of thickness d (300 nm), charge carriers at the boundaries should be quenched because of the high density of trap states. Therefore, eq 6 can be solved with the boundary conditions: $N_t(x,\omega) = 0$; $x = 0, d$, viz.

$$N_t(x,\omega) = B_1(\omega,T)\, e^{K_1x} - B_2(\omega,T)\, e^{-K_1x} + \left[\frac{K_2(T,\beta)}{K_1^2(T,\omega) - \beta}\right] e^{-\beta x} \quad (7)$$

where the parameters are defined as

$$K_1^2(T;\omega) = \frac{1}{D_h(T)}\left\{i\omega + \frac{1}{\tau_E(T)} - \frac{R_T}{[1+A(T)][1+i\omega\tau_i(T)]}\right\}$$

DOI: 10.1021/acs.jpcc.7b11933
J. Phys. Chem. C 2018, 122, 5759−5766

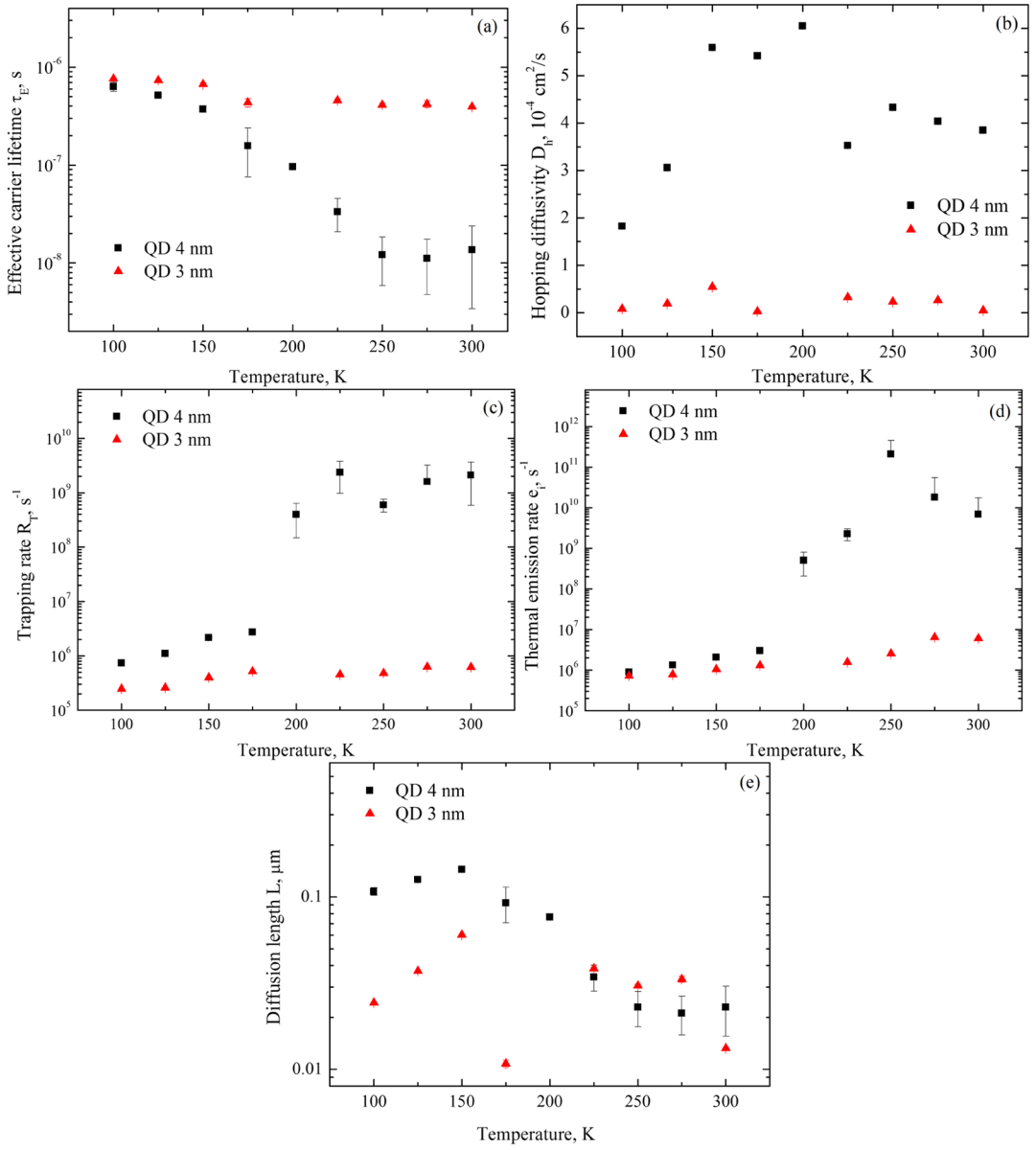

Figure 9. Best-fitted exciton (or dissociated photocarrier) transport parameters of the two PbS CQD thin films (sample A: 3 nm and sample B: 4 nm). (a) Effective carrier lifetime τ_e; (b) carrier hopping diffusivity D_h; (c) trapping rate R_T; (d) thermal emission rate e_i; and (e) diffusion length L.

$$K_2(T, \beta) = \frac{G_0\beta}{D_h(T)[1 + A(T)]}$$

$$B_1(\omega, T) = \left[\frac{K_2(T, \beta)}{K_1^2(T, \omega) - \beta^2}\right]\left(\frac{e^{-K_1 d} - e^{-\beta d}}{e^{K_1 d} - e^{-K_1 d}}\right)$$

$$B_2(\omega, T) = \left[\frac{K_2(T, \beta)}{K_1^2(T, \omega) - \beta^2}\right]\left(\frac{e^{K_1 d} - e^{-\beta d}}{e^{K_1 d} - e^{-K_1 d}}\right)$$

The PCR signal can be expressed as an integral of the charge carrier population over the thickness of the CQD layer:

$$S(\omega) = F(\lambda_1, \lambda_2)\int_0^d N_i(x, \omega)\, dx \tag{8}$$

Here, $F(\lambda_1,\lambda_2)$ is an instrumentation coefficient which depends on the spectral emission bandwidth $[\lambda_1,\lambda_2]$ of the InGaAs detector.[21] Therefore, the final expression for the PCR signal can be obtained:

$$\frac{S(\omega)}{F(\lambda_1, \lambda_2)} = \left[\frac{K_2(T, \beta)}{\beta^2 - K_1^2(T, \omega)}\right]\left\{\frac{(1 + e^{-\beta d})}{K_1(1 - e^{-2K_1 d})} - \frac{1}{\beta}(1 - e^{-\beta d})\right\} \tag{9}$$

Figure 8 shows the experimental PCR phase frequency scans at various temperatures for the two samples and the best fits to phase curves derived from eq 9. PCR phase lags increase at high frequencies, but it is obvious that the two samples exhibit different temperature responses. In sample A, the phase curves are very close to each other at all temperatures, indicating that carrier lifetime shows weak temperature dependence. However, in sample B, the phase curves peel off at lower "knee" frequencies at all temperatures in a manner similar to those in our previous reports,[22,23] indicating that carrier lifetime in sample B is longer than that in sample A and increases substantially with decreasing temperature.

DOI: 10.1021/acs.jpcc.7b11933
J. Phys. Chem. C 2018, 122, 5759−5766

Amplitude trends with temperature are more complicated than phases as they include relative contributions from trap emissions and nonradiative de-excitation pathways that affect the relative radiative emission rates and amplitude levels at low frequencies, unlike the phase curves which all converge to zero phase shifts.

Figure 9 shows the extracted temperature-dependent five carrier transport parameters: τ_E, D_h, R_T, e_i, and diffusion length L for samples A and B. With increasing temperature from 100 to 300 K, the best-fitted effective carrier lifetime decreases dramatically in sample B, whereas it almost remains unchanged in sample A. The extracted values are comparable to previously reported values.[22,23] The hopping diffusivity D_h is found to be in the range from 1×10^{-4} to 6×10^{-4} cm^2/s in sample B and from 7×10^{-6} to 5×10^{-5} cm^2/s in sample A, which fall within the range calculated by Hu et al. for PbS−MAPbI$_3$ CQDs.[23] It is concluded that excitons or dissociated carriers in sample B have better hopping ability, whereas carriers in sample A are more likely to decay locally. It can be seen from Figure 9c,d that, despite its higher hopping diffusivity, sample B exhibits much higher trapping rate R_T and thermal emission rate e_i than sample A, especially at high temperatures, which is consistent with nonradiative processes dominating excitonic and/or dissociated carrier lifetimes in sample B, as per Figure 9a. The diffusion length $L = \sqrt{D_h \tau_E}$ controls the exciton diffusion rate away from the generation location. Figure 9e shows that L is much higher in sample B, dominated by the higher diffusivity, exhibiting nonmonotonic trends with temperature in both samples. L decreases at high temperatures because lifetime decreases, and its values converge at $T > 200$ K in both samples as higher diffusivity in B counterbalances the higher lifetime in A. This trade-off would tend to diminish very large external current density generation differences between devices fabricated with the two sizes of QDs for room-temperature operation. Given these considerations, it is clear that the smaller size (3 nm) QD sample may be more suitable for use in the fabrication of optoelectronic devices such as CQD solar cells because it exhibits lower trapping rates, longer lifetimes, and lower nonradiative de-excitation rates over the entire temperature range, including room temperature.

4. CONCLUSIONS

In summary, exciton dynamics in PbS CQD thin films were studied by combining comprehensive results of temperature-dependent PL spectroscopy and PCR amplitude and phase frequency dependencies. PL bands were analyzed using line shape analysis, and important carrier transport parameters were extracted from the PCR frequency responses with a trap-state-mediated carrier hopping transport model. The only difference during the preparation process of the two samples was the QD size. Unexpected differences of the exciton de-excitation properties were clearly found. Secondary PL bands originating in defect states were found in sample A, whereas strong nonradiative effects were observed from the PCR measurements in sample B, which was expected to have better surface quality as indicated from the PL spectra. Enhanced PL emission at high temperatures was found for both samples because of thermally activated exciton redistributions from dark trap states to emission states.

AUTHOR INFORMATION

Corresponding Author

*E-mail: s.j19851230@163.com.

ORCID

Jing Wang: 0000-0001-7417-9777

Notes

The authors declare no competing financial interest.

ACKNOWLEDGMENTS

A.M. is grateful to the Foundation for Innovative Research Groups of the National Natural Science Foundation of China (grant no. 61421002). He also acknowledges the Natural Sciences and Engineering Research Council (NSERC) for a Discovery Grant, the Canada Foundation for Innovation (CFI) for equipment grants, the Canada Research Chairs Program, and the Chinese Recruitment Program of Global Experts (Thousand Talents). J.W. is grateful to the National Natural Science Foundation of China (grant nos. 61704023, 61601092, and 61771103).

REFERENCES

(1) Sun, Z.; Liu, Z.; Li, J.; Tai, G.a.; Lau, S.-P.; Yan, F. Infrared Photodetectors Based on CVD-Grown Graphene and PbS Quantum Dots with Ultrahigh Responsivity. *Adv. Mater.* **2012**, *24*, 5878−5883.

(2) Kufer, D.; Nikitskiy, I.; Lasanta, T.; Navickaite, G.; Koppens, F. H. L.; Konstantatos, G. Hybrid 2D-0D MoS_2-PbS Quantum Dot Photodetectors. *Adv. Mater.* **2015**, *27*, 176−180.

(3) Sun, L.; Choi, J. J.; Stachnik, D.; Bartnik, A. C.; Hyun, B.-R.; Malliaras, G. G.; Hanrath, T.; Wise, F. W. Bright Infrared Quantum-Dot Light-Emitting Diodes through Inter-Dot Spacing Control. *Nat. Nanotechnol.* **2012**, *7*, 369−373.

(4) Mueller, A. H.; Petruska, M. A.; Achermann, M.; Werder, D. J.; Akhadov, E. A.; Koleske, D. D.; Hoffbauer, M. A.; Klimov, V. I. Multicolor Light-Emitting Diodes Based on Semiconductor Nanocrystals Encapsulated in GaN Charge Injection Layers. *Nano Lett.* **2005**, *5*, 1039−1044.

(5) Tang, J.; Kemp, K. W.; Hoogland, S.; Jeong, K. S.; Liu, H.; Levina, L.; Furukawa, M.; Wang, X.; Debnath, R.; Cha, D. Colloidal-Quantum-Dot Photovoltaics Using Atomic-Ligand Passivation. *Nat. Mater.* **2011**, *10*, 765−771.

(6) McDonald, S. A.; Konstantatos, G.; Zhang, S.; Cyr, P. W.; Klem, E. J. D.; Levina, L.; Sargent, E. H. Solution-Processed PbS Quantum Dot Infrared Photodetectors and Photovoltaics. *Nat. Mater.* **2005**, *4*, 138−142.

(7) Gur, I.; Fromer, N. A.; Geier, M. L.; Alivisatos, A. P. Air-Stable All-Inorganic Nanocrystal Solar Cells Processed from Solution. *Science* **2005**, *310*, 462−465.

(8) Gao, J.; Zhang, J.; de Lagemaat, J. V.; Johnson, J. C.; Beard, M. C. Charge Generation in PbS Quantum Dot Solar Cells Characterized by Temperature-Dependent Steady-State Photoluminescence. *ACS Nano* **2014**, *8*, 12814.

(9) Romero, H. E.; Drndic, M. Coulomb Blockade and Hopping Conduction in PbSe Quantum Dots. *Phys. Rev. Lett.* **2005**, *95*, 156801.

(10) Ren, F.; Lindley, S. A.; Zhao, H.; Tan, L.; Gonfa, B. A.; Pu, Y.-C.; Yang, F.; Liu, X.; Vidal, F.; Zhang, J. Z.; et al. Towards Understanding the Unusual Photoluminescence Intensity Variation of Ultrasmall Colloidal Pbs Quantum Dots with the Formation of a Thin CdS Shell. *Phys. Chem. Chem. Phys.* **2016**, *18*, 31828.

(11) Marshall, A. R.; Beard, M. C.; Johnson, J. C. Nongeminate Radiative Recombination of Free Charges in Cation-Exchanged PbS Quantum Dot Films. *Chem. Phys.* **2016**, *471*, 75−80.

(12) Stavrinadis, A.; Pradhan, S.; Papagiorgis, P.; Itskos, G.; Konstantatos, G. Suppressing Deep Traps in PbS Colloidal Quantum Dots via Facile Iodide Substitutional Doping for Solar Cells with Efficiency >10%. *ACS Energy Lett.* **2017**, *2*, 739−744.

(13) Litvin, A. P.; Parfenov, P. S.; Ushakova, E. V.; Vorsina, T. A.; Gamboa, A. L. S.; Fedorov, A. V.; Baranov, A. V. FRET-Activated Delayed Fluorescence in Densely Packed PbS Quantum-Dot Ensembles. *J. Phys. Chem. C* **2015**, *119*, 17016−17022.

DOI: 10.1021/acs.jpcc.7b11933
J. Phys. Chem. C 2018, 122, 5759−5766

(14) Chuang, C.-H. M.; Maurano, A.; Brandt, R. E.; Hwang, G. W.; Jean, J.; Buonassisi, T.; Bulović, V.; Bawendi, M. G. Open-Circuit Voltage Deficit, Radiative Sub-Bandgap States, and Prospects in Quantum Dot Solar Cells. *Nano Lett.* **2015**, *15*, 3286−3294.
(15) Litvin, A. P.; Parfenov, P. S.; Ushakova, E. V.; Gamboa, A. L. S.; Fedorov, A. V.; Baranov, A. V. Size and Temperature Dependencies of the Low-Energy Electronic Structure of PbS Quantum Dots. *J. Phys. Chem. C* **2014**, *118*, 20721−20726.
(16) Poulikakos, L. V.; Prins, F.; Tisdale, W. A. Transition from Thermodynamic to Kinetic-Limited Excitonic Energy Migration in Colloidal Quantum Dot Solids. *J. Phys. Chem. C* **2014**, *118*, 7894−7900.
(17) Miyazaki, J. Quantifying Exciton Hopping in Disordered Media with Quenching Sites: Application to Arrays of Quantum Dots. *Phys. Rev. B: Condens. Matter Mater. Phys.* **2013**, *88*, 155302.
(18) Rinnerbauer, V.; Egelhaaf, H.-J.; Hingerl, K.; Zimmer, P.; Werner, S.; Warming, T.; Hoffmann, A.; Kovalenko, M.; Heiss, W.; Hesser, G.; Schaffler, F. Energy Transfer in Close-Packed PbS Nanocrystal Films. *Phys. Rev. B: Condens. Matter Mater. Phys.* **2008**, *77*, 085322.
(19) Andreakou, P.; Brossard, M.; Li, C.; Bernechea, M.; Konstantatos, G.; Lagoudakis, P. G. Size- and Temperature-Dependent Carrier Dynamics in Oleic Acid Capped PbS Quantum Dots. *J. Phys. Chem. C* **2013**, *117*, 1887−1892.
(20) Ma, J.; Ji, X.; Wang, G.; Wei, X.; Lu, H.; Yi, X.; Duan, R.; Wang, J.; Zeng, Y.; Li, J. Anomalous Temperature Dependence of Photoluminescence in Self-Assembled InGaN Quantum Dots. *Appl. Phys. Lett.* **2012**, *101*, 131101.
(21) Mandelis, A.; Batista, J.; Shaughnessy, D. Infrared Photo-carrier Radiometry of Semiconductors: Physical Principles, Quantitative Depth Profilometry and Scanning Imaging of Deep Sub-surface Electronic Defects. *Phys. Rev. B* **2003**, *67*, 205208.
(22) Wang, J.; Mandelis, A.; Melnikov, A.; Hoogland, S.; Sargent, E. H. Exciton Lifetime Broadening and Distribution Profiles of PbS Colloidal Quantum Dot Thin Films Using Frequency- and Temperature-Scanned Photocarrier Radiometry. *J. Phys. Chem. C* **2013**, *117*, 23333−23348.
(23) Hu, L.; Mandelis, A.; Yang, Z.; Guo, X.; Lan, X.; Liu, M.; Walters, G.; Melinkov, A.; Melnikov, A.; Sargent, E. H. Temperature- and Ligand-Dependent Carrier Transport Dynamics in Photovoltaic PbS Colloidal Quantum Dot Thin Films Using Diffusion-Wave Methods. *Sol. Energy Mater. Sol. Cells* **2017**, *164*, 135−145.
(24) Kang, I.; Wise, F. W. Electronic Structure and Optical Properties of PbS and PbSe Quantum Dots. *J. Opt. Soc. Am. B* **1997**, *14*, 1632−1646.
(25) Pendyala, N. B.; Rao, K. S. R. K. Identification of Surface States in PbS Quantum Dots by Temperature Dependent Photoluminescence. *J. Lumin.* **2008**, *128*, 1826−1830.
(26) Kigel, A.; Brumer, M.; Maikov, G. I.; Sashchiuk, A.; Lifshitz, E. Thermally Activated Photoluminescence in Lead Selenide Colloidal Quantum Dots. *Small* **2009**, *5*, 1675−1681.
(27) Gaponenko, M. S.; Lutich, A. A.; Tolstik, N. A.; Onushchenko, A. A.; Malyarevich, A. M.; Petrov, E. P.; Yumashev, K. V. Temperature-Dependent Photoluminescence of PbS Quantum Dots in Glass: Evidence of Exciton State Splitting and Carrier Trapping. *Phys. Rev. B: Condens. Matter Mater. Phys.* **2010**, *82*, 125320.
(28) Madelung, O. Group VI Elements. *Semiconductors: Data Handbook*; Springer: Berlin, 2004; pp 419−433.
(29) Olkhovets, A.; Hsu, R.-C.; Lipovskii, A.; Wise, F. W. Size-Dependent Temperature Variation of The Energy Gap in Lead-Salt Quantum Dots. *Phys. Rev. Lett.* **1998**, *81*, 3539−3542.
(30) Wang, J.; Mandelis, A.; Melnikov, A.; Sun, Q. Trap State Effects in PbS Colloidal Quantum Dot Exciton Kinetics Using Photocarrier Radiometry Intensity and Temperature Measurements. *Int. J. Thermophys.* **2016**, *37*, 60.
(31) Ushakova, E. V.; Litvin, A. P.; Parfenov, P. S.; Fedorov, A. V.; Artemyev, M.; Prudnikau, A. V.; Rukhlenko, I. D.; Baranov, A. V. Anomalous Size-Dependent Decay of Low-Energy Luminescence from PbS Quantum Dots in Colloidal Solution. *ACS Nano* **2012**, *6*, 8913−8921.

DOI: 10.1021/acs.jpcc.7b11933
J. Phys. Chem. C 2018, 122, 5759−5766